LOW-LYING BARYON RESONANCES FROM LATTICE QCD*

Colin Morningstar

Department of Physics, Carnegie Mellon University
Pittsburgh, Pennsylvania 15213, USA

Received 7 October 2025, accepted 29 October 2025, published online 10 February 2026

Calculating the properties of baryon resonances from quantum chromodynamics requires evaluating the temporal correlations between hadronic operators using integrations over field configurations weighted by a phase associated with the action. By formulating quantum chromodynamics on a space-time lattice in imaginary time, such integrations can be carried out non-perturbatively using a Markov-chain Monte Carlo method with importance sampling. The energies of stationary states in the finite volume of the lattice can be extracted from the temporal correlations. A quantization condition involving the scattering K-matrix and a complicated "box matrix" also yields a finite-volume energy spectrum. By appropriately parametrizing the scattering K-matrix, the best-fit values of the K-matrix parameters are those that produce a finite-volume spectrum which most closely matches that obtained from the Monte Carlo computations. Results for the Δ resonance are presented, and a study of scattering for energies near the $\Lambda(1405)$ resonance is outlined, showing a two-pole structure. The prospects for applying this methodology to the Roper resonance are discussed.

DOI:10.5506/APhysPolB.57.2-A10

1. Introduction

The interactions between quarks and gluons are described by quantum chromodynamics (QCD) [1], a quantum field theory based on a non-Abelian local SU(3) gauge symmetry. Quarks and gluons are not directly observable, but they bind to form composite particles known as hadrons, such as protons, neutrons, and pions, which can be observed in experiments. The majority of hadrons are scattering resonances, unstable short-lived particles. The famous Roper resonance [2] is the lightest excitation of the proton.

The interactions between hadrons and the formation of hadron resonances are also described by QCD. Unfortunately, extracting the properties of bound states and resonances is difficult in relativistic quantum field theories,

and the strong coupling nature of QCD much exacerbates this difficulty. Calculating the properties of hadron resonances from quantum chromodynamics requires evaluating the temporal correlations between hadronic operators using integrations over field configurations weighted by a phase associated with the action. Standard perturbative techniques which work well in quantum electrodynamics for performing such integrals are nearly useless for the integrals which must be evaluated in QCD. By formulating QCD on a space-time lattice in imaginary time, such integrations can be carried out non-perturbatively using a Markov-chain Monte Carlo method with importance sampling. The use of such techniques is broadly known as lattice QCD.

In recent years, lattice QCD has advanced to the point where it can now determine the masses and decay widths of unstable hadronic resonances, such as the ρ and $\Lambda(1405)$. These calculations begin by evaluating the finite-volume energy levels of the multi-hadron states into which the resonances decay, using Markov-chain Monte Carlo techniques for the integration over the fields. Next, parametrized models of the scattering amplitudes are constructed and inserted into a well-established quantization condition. This condition involves the scattering K-matrix and a complicated "box matrix", which together produce a finite-volume spectrum that depends on the scattering parameters. By adjusting these parameters to best reproduce the energy levels obtained from lattice QCD, the properties of the resonances can be extracted from the resulting scattering amplitudes.

A critical component of these calculations is determining the energies of stationary states in a finite volume, particularly those involving multi-hadron contributions. These energies are obtained from Monte Carlo estimates of time-dependent correlation functions built from carefully designed quantum field operators that generate the desired states. To compute these correlators, quark propagators from various lattice source points must be contracted together. These propagators are inverses of extremely large matrices, but only their products with specific source vectors are required. For single-hadron operators, translational symmetry allows the use of a limited number of source sites. However, multi-hadron operators necessitate the inclusion of all spatial sites on a given source time slice, making reliable estimates difficult. This challenge has been overcome with new methods, such as the Laplacian–Heaviside (LapH) quark-field smearing. The LapH smearing reduces the computational burden by projecting the quark propagators into a smaller subspace defined by eigenvectors of the gauge-covariant Laplacian, enabling feasible use of all spatial sites.

This report showcases some of our recent lattice QCD results on baryon resonances. The results from a study of the Δ resonance are presented, and an investigation into the two-pole structure near the $\Lambda(1405)$ is described. The feasibility of studying the famous Roper resonance in the near future is discussed.

2. Outline of methodology

To study resonance and scattering properties in lattice QCD, one first evaluates the finite-volume energies of stationary states corresponding to the relevant decay products for a variety of total momenta and symmetry representations. The first step in determining these stationary-state energies is to evaluate an $N \times N$ Hermitian matrix of temporal correlations $C_{ij}(t) = \langle 0 | \, O_i(t + t_0) \, \bar{O}_j(t_0) \, | 0 \rangle$ for each total momentum and symmetry representation. These correlations involve judiciously designed operators $O_j(t) = O_j[\bar{\psi}, \psi, U]$ comprised of quark $\psi, \bar{\psi}$, and gluon U field operators which create the states of interest. Each temporal correlator can be expressed as a ratio of path integrals over the fields

$$C_{ij}(t) = \frac{\int \mathcal{D}\left(\bar{\psi}, \psi, U\right) \quad O_i(t + t_0) \; \bar{O}_j(t_0) \; \exp\left(-S\left[\bar{\psi}, \psi, U\right]\right)}{\int \mathcal{D}\left(\bar{\psi}, \psi, U\right) \; \exp\left(-S\left[\bar{\psi}, \psi, U\right]\right)} \,, \tag{1}$$

where the action in imaginary time has the form

$$S\left[\bar{\psi}, \psi, U\right] = \bar{\psi} \; K[U] \; \psi + S_G[U] \,, \tag{2}$$

and where $K[U]$ is the fermion Dirac matrix and $S_G[U]$ is the gluon action. The integrals over the Grassmann-valued quark/antiquark fields can be done exactly, leaving expressions of the form

$$C_{ij}(t) = \frac{\int \mathcal{D}U \;\; \det K[U] \;\; \left(K^{-1}[U] \ldots K^{-1}[U] + \ldots\right) \;\; \exp\left(-S_G[U]\right)}{\int \mathcal{D}U \;\; \det K[U] \;\; \exp\left(-S_G[U]\right)} \,. \tag{3}$$

For the remaining integrations over the gluon fields, the Monte Carlo method is used. This requires formulating QCD on a space-time lattice (usually hypercubic), with quark fields residing on the sites and the gluon field residing on the links between lattice sites. The lattice QCD action is formulated in such a way so as to maintain local gauge invariance [3]. A Markov chain is used to generate a sequence of gauge-field configurations $U_1, U_2, \ldots, U_N$ using the Metropolis method [4] with a complicated global updating proposal, such as RHMC [5], which proposes a new gauge field by selecting conjugate momenta randomly chosen with Gaussian distributions and evolving the fields in a fictitious time variable using Hamilton equations. The proposed field differs globally from the current field, but the value of its action is very near that of the current field, ensuring a high acceptance rate. The fermionic determinants $\det K$ are usually estimated using a multivariate Gaussian integral over so-called pseudo-fermion fields. The correlators are then estimated using the ensemble of gauge configurations generated by the above procedure. Systematic errors include discretization and finite-volume effects. To speed up computations, unphysically large quark masses are often used.

An efficient way to construct single-hadron operators is to assemble them using covariantly-displaced smeared quark fields as building blocks. Stout link smearing [6] is used for the gauge field links $\widetilde{U}_j(x)$, and the Laplacian–Heaviside (LapH) [7, 8] smearing is used for the quark fields

$$\widetilde{\psi}_{a\alpha}(x) = \mathcal{S}_{ab}(x,y)\ \psi_{b\alpha}(y)\,, \qquad \mathcal{S} = \Theta\left(\sigma_{\rm s}^2 + \widetilde{\Delta}\right)\,, \tag{4}$$

where $\widetilde{\Delta}$ denotes a 3-dimensional gauge-covariant Laplacian defined in terms of the stout links $\widetilde{U}$ and $\sigma_{\rm s}$ is the smearing cutoff. Displaced quark fields are defined by

$$q^A_{a\alpha j} = D^{(j)}\widetilde{\psi}^{(A)}_{a\alpha}\,, \qquad \bar{q}^A_{a\alpha j} = \widetilde{\bar{\psi}}^{(A)}_{a\alpha}\,\gamma_4\,D^{(j)\dagger}\,, \tag{5}$$

where the displacement $D^{(j)}$ is a product of smeared links

$$D^{(j)}\left(x,x'\right) = \widetilde{U}_{j_1}(x)\ \widetilde{U}_{j_2}(x{+}d_2)\ \widetilde{U}_{j_3}(x{+}d_3)\ldots\widetilde{U}_{j_p}(x{+}d_p)\delta_{x',\ x+d_{p+1}}\,. \tag{6}$$

In the above equations, a, b are color indices, α is a Dirac spin index, and j labels a displacement path of gauge links in directions $j_1, j_2, \ldots$ A variety of displacements can be used to build up the needed orbital and radial structure, as shown in Fig. 1. So-called elemental quark–antiquark and three-quark operators which create a definite momentum $\boldsymbol{p}$ are defined by

$$\bar{\Phi}^{AB}_{\alpha\beta}(\boldsymbol{p},t) \;=\; \sum_{\boldsymbol{x}} \mathrm{e}^{i\boldsymbol{p}\cdot\left(\boldsymbol{x}+\frac{1}{2}\left(\boldsymbol{d}_\alpha+\boldsymbol{d}_\beta\right)\right)}\delta_{ab}\ \bar{q}^B_{b\beta}(\boldsymbol{x},t)\ q^A_{a\alpha}(\boldsymbol{x},t)\,, \tag{7}$$

$$\bar{\Phi}^{ABC}_{\alpha\beta\gamma}(\boldsymbol{p},t) \;=\; \sum_{\boldsymbol{x}} \mathrm{e}^{i\boldsymbol{p}\cdot\boldsymbol{x}}\varepsilon_{abc}\ \bar{q}^C_{c\gamma}(\boldsymbol{x},t)\ \bar{q}^B_{b\beta}(\boldsymbol{x},t)\ \bar{q}^A_{a\alpha}(\boldsymbol{x},t)\,. \tag{8}$$

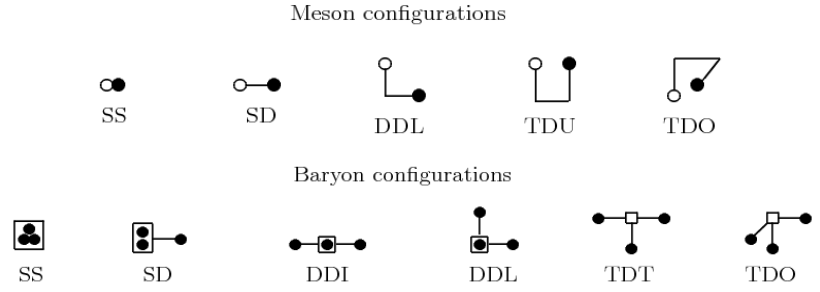

Fig. 1. The spatial arrangements of the quark–antiquark meson operators (top) and the three-quark baryon operators (bottom) that we use. Smeared quark fields are shown as solid circles, each hollow circle indicates a smeared antiquark field, the solid line segments indicate covariant displacements, and each hollow box indicates the location of a Levi-Civita color coupling.

In these operators, A, B, C are quark flavor indices, a, b, c are color indices, $\boldsymbol{d}_\alpha, \boldsymbol{d}_\beta$ are the spatial displacements of the $q, \bar{q}$ fields, respectively, from site $\boldsymbol{x}$, and α, β, γ denote compound indices incorporating both a Dirac spin index and a displacement path. Group theoretical projections onto the irreducible representations (irreps) of the lattice symmetry group are then employed to create the final single meson and single baryon operators

$$\bar{M}_l(t) = c^{(l)*}_{\alpha\beta}\ \bar{\Phi}^{AB}_{\alpha\beta}(t)\,, \qquad \bar{B}_l(t) = c^{(l)*}_{\alpha\beta\gamma}\ \bar{\Phi}^{ABC}_{\alpha\beta\gamma}(t)\,. \tag{9}$$

In the above, α, β, γ again indicate compound indices incorporating both a Dirac spin index and a displacement path, and l is the final index which labels the hadron operator.

Implementing two- and three-hadron operators as appropriate superpositions of products of the single-hadron operators of definite momenta is straightforward

$$c^{I_{3a} I_{3b}}_{\boldsymbol{p}_a \lambda_a;\ \boldsymbol{p}_b \lambda_b}\ B^{I_a I_{3a} S_a}_{\boldsymbol{p}_a \Lambda_a \lambda_a i_a}\ B^{I_b I_{3b} S_b}_{\boldsymbol{p}_b \Lambda_b \lambda_b i_b} \tag{10}$$

for the fixed total momentum $\boldsymbol{p} = \boldsymbol{p}_a + \boldsymbol{p}_b$ and fixed $\Lambda_a, i_a, \Lambda_b, i_b$. Group theory projections onto the little group of $\boldsymbol{p}$ and isospin irreps are then carried out. It is very important to specify all phases of the single-hadron operators for all momenta, and this is generally done by selecting a reference momentum direction $\boldsymbol{p}_{\rm ref}$, then for each momentum $\boldsymbol{p}$, selecting one reference rotation $R^{\boldsymbol{p}}_{\rm ref}$ that transforms $\boldsymbol{p}_{\rm ref}$ into $\boldsymbol{p}$. This method creates large numbers of multi-hadron operators very efficiently.

Once the temporal correlations are obtained, their spectral representations can be used to extract the stationary-state energies

$$C_{ij}(t) = \sum_n Z^{(n)}_i Z^{(n)*}_j\ \mathrm{e}^{-E_n t}\,, \qquad Z^{(n)}_j = \langle 0|\ O_j\ |n\rangle\,, \tag{11}$$

which neglects small temporal wrap-around contributions, where the energies E_n are discrete in a finite volume. Given the large number of complex parameters in Eq. (11), it is not feasible to fit the entire correlation matrix using Eq. (11). Some method of rotating or diagonalizing the matrix is needed to make the extraction of the energies and overlap factors by least-squares fitting practical. The use of variational techniques to assist with this dates back to Refs. [9–12]. The way we proceed is to define a new correlation matrix $\widetilde{C}(t)$ using a single rotation

$$\widetilde{C}(t) = U^\dagger\ C(\tau_0)^{-1/2}\ C(t)\ C(\tau_0)^{-1/2}\ U\,, \tag{12}$$

where the columns of U are the eigenvectors of $C(\tau_0)^{-1/2}\, C(\tau_D)\, C(\tau_0)^{-1/2}$. One then chooses τ_0 and τ_D large enough so $\widetilde{C}(t)$ remains diagonal for $t > \tau_D$

within statistical errors. Two-exponential fits to the diagonal rotated correlators $\widetilde{C}_{\alpha\alpha}(t)$ then yield the energies E_α and overlaps $Z_j^{(n)}$. Energy shifts from non-interacting values can also be obtained from single exponential fits to a suitable ratio of correlators, but such fits must be cautiously done in combination with fits to correlators that are not ratios.

The usefulness of Eq. (12) can be demonstrated using a simple toy model example. In this example, there are $N_{\rm eig} = 200$ eigenstates $|n\rangle$ for $n = 0, 1, \ldots, N_{\rm eig} - 1$, and the energies are taken to be

$$E_0 = 0.20\,, \qquad E_n = E_{n-1} + \frac{0.08}{\sqrt{n}}\,, \qquad n = 1, 2, \ldots, N_{\rm eig} - 1\,. \tag{13}$$

This example studies an $N \times N$ correlator matrix, where $N = 12$. A set of operators is selected such that each operator is expected to predominantly create a different eigenstate, so the overlaps of the $j^{\rm th}$ operator onto the eigenstates is taken to be

$$Z_j^{(n)} = \frac{(-1)^{j+n}}{1 + 0.05(j-n)^2}\,. \tag{14}$$

The so-called "effective energies" associated with the diagonal elements of the original raw correlator matrix of this toy model are shown in Fig. 2 (a). Each effective energy is defined by

$$E_{\rm eff}^{(n)}(t) = \ln\left(\frac{C_{nn}(t)}{C_{nn}(t+1)}\right)\,. \tag{15}$$

Each of these effective energies eventually tends down to $E_0 = 0.20$ since the state created by each operator has some overlap with the lowest-lying eigenstate $|0\rangle$. As the operator index increases, the couplings to higher-lying eigenstates get larger, so one sees that the effective energies associated with those operators have higher values at smaller times.

The effective energies associated with the eigenvalues $\lambda_n(t)$ of $C(t)$ are shown in Fig. 2 (b). Each of these effective energies is defined by

$$E_{\rm eff}^{{\rm eig}(n)}(t) = \ln\left(\frac{\lambda_n(t)}{\lambda_n(t+1)}\right)\,. \tag{16}$$

To order the eigenvalues for different t values, eigenvector "pinning" has been used. For one reference value of time $t_{\rm ref}$, a particular order of the eigenvalues has been chosen, and the eigenvectors associated with these eigenvalues are used as references. For a different value of time $t \neq t_{\rm ref}$, the inner products of the eigenvectors at t are taken with those at the reference time $t_{\rm ref}$, and the eigenvalue associated with the eigenvector at time t with maximal overlap

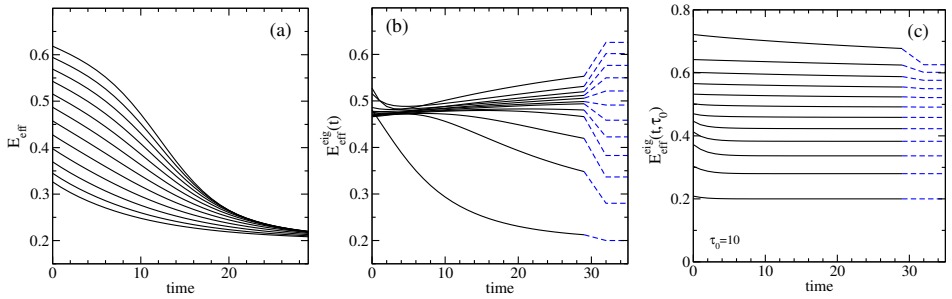

Fig. 2. (a) Effective energies associated with the diagonal elements of the original raw correlator matrix $C(t)$ of the toy model, whose energies are defined in Eq. (13) and the overlaps in Eq. (14). (b) Effective energies associated with the eigenvalues of the original correlator matrix $C(t)$ with eigenvector pinning used to label or order the eigenvalues. (c) Effective energies associated with the eigenvalues of $C(\tau_0)^{-1/2}C(t)C(\tau_0)^{-1/2}$ with eigenvector pinning, for $\tau_0 = 10$.

onto the reference eigenvector n is identified as $\lambda_n(t)$. The dashed blue lines indicate the lowest 12 exact energies. These effective energies will eventually tend toward the horizontal dashed blue lines, but certainly by $t = 30$, most of these effective energies still significantly disagree with their expected large-t values. Also, many of the curves cross each other, and the curves are very close to one another for small and moderate t values. Clearly, trying to extract the spectrum of energies from the eigenvalues of $C(t)$ will be a difficult task.

The effective energies associated with the eigenvalues $\lambda_n(t, \tau_0)$ of the modified correlator matrix $C(\tau_0)^{-1/2}C(t)C(\tau_0)^{-1/2}$ are shown in Fig. 2 (c) for $\tau_0 = 10$. Each of these effective energies is defined by

$$E_{\rm eff}^{{\rm eig}(n)}(t, \tau_0) = \ln\left(\frac{\lambda_n(t, \tau_0)}{\lambda_n(t+1, \tau_0)}\right) . \tag{17}$$

To order the eigenvalues, eigenvector "pinning" has again been used. The dashed blue lines indicate the lowest 12 exact energies. These effective energies look dramatically different from those in Fig. 2 (b). The approach of these effective energies to the dashed blue lines is dramatically faster, and no crossings of the curves are observed. By time $t = 30$, the lower-lying levels already agree with their expected large-t values, and only a few of the levels near N still exhibit a significant difference from its limiting blue line. These results clearly show the great superiority of using the eigenvalues of $C(\tau_0)^{-1/2}C(t)C(\tau_0)^{-1/2}$ instead of $C(t)$. If one varies τ_0, one finds that the

results are insensitive to the value of τ_0. One also sees that if N levels are desired, then a correlator matrix larger than $N \times N$ should be used, such as $\frac{3}{2}N \times \frac{3}{2}N$.

The relationship of the finite-volume energies obtained in lattice QCD and the infinite-volume scattering S-matrix was first studied in detail in Refs. [13, 14], but lattice QCD computations at that time could not determine the energies of multi-hadron states reliably and accurately enough to take advantage of this relationship. As the lattice QCD methodology improved for multi-hadron operators, the relationship between scattering amplitudes and finite-volume stationary-state energies was revisited in Refs. [15, 16], limiting attention to a single channel of identical spinless particles. Later works generalized their results to treat multi-channels with different particle masses and non-zero spins [17]. Our procedure for evaluating scattering phase shifts from lattice QCD energies is presented in Ref. [18] and is summarized below.

Instead of the unitary S-matrix, the real and symmetric K-matrix [19, 20], defined using the S-matrix by

$$S = (1 + iK)(1 - iK)^{-1} = (1 - iK)^{-1}(1 + iK)\,, \tag{18}$$

is usually used in the quantization condition that relates the scattering amplitudes and the finite-volume energies since it is easier to parametrize a real symmetric matrix than a unitary matrix. Rotational invariance implies that

$$\big\langle J' m_{J'} L' S' a' \big|\; K \;\big| J m_J L S a \big\rangle = \delta_{J'J} \delta_{m_{J'} m_J}\; K^{(J)}_{L'S'a';\; LSa}(E_{\rm cm})\,. \tag{19}$$

We use an orthonormal basis of states, each labeled $|Jm_JLSa\rangle$, where J is the total angular momentum of the two particles in the center-of-momentum frame, m_J is the projection of the total angular momentum onto the z-axis, L is the orbital angular momentum of the two particles in the center-of-momentum frame (not to be confused with the lattice length L_b here), and S in the basis vector is the total spin of the two particles (not the scattering matrix). The multichannel generalization [21–23] of the effective range expansion (ERE) is

$$K^{-1(J)}_{L'S'a';\; LSa}(E_{\rm cm}) = q_{{\rm cm},a'}^{\,-L'-\frac{1}{2}}\; \widetilde{K}^{-1(J)}_{L'S'a';\; LSa}(E_{\rm cm})\; q_{{\rm cm},a}^{\,-L-\frac{1}{2}}\,, \tag{20}$$

where $\widetilde{K}^{-1(J)}_{L'S'a';\; LSa}(E_{\rm cm})$ is a real, symmetric, and often analytic function of the center-of-momentum energy $E_{\rm cm}$. For a given total momentum $\boldsymbol{P} = (2\pi/L_b)\boldsymbol{d}$ in a spatial L_b^3 volume with periodic boundary conditions, where $\boldsymbol{d}$ is a vector of integers, we determine the total lab-frame energy E for a two-particle interacting state in our lattice QCD simulations. If the masses

of the two particles in the decay channel a are m_{1a} and m_{2a}, we boost to the center-of-mass frame and define

$$E_{\rm cm} = \sqrt{E^2 - \boldsymbol{P}^2}\,, \qquad \gamma = \frac{E}{E_{\rm cm}}\,, \tag{21}$$

$$\boldsymbol{q}^2_{{\rm cm},a} = \frac{1}{4}E^2_{\rm cm} - \frac{1}{2}\left(m^2_{1a} + m^2_{2a}\right) + \frac{\left(m^2_{1a} - m^2_{2a}\right)^2}{4E^2_{\rm cm}}\,,$$

$$u^2_a = \frac{L^2\boldsymbol{q}^2_{{\rm cm},a}}{(2\pi)^2}\,, \qquad \boldsymbol{s}_a = \left(1 + \frac{\left(m^2_{1a} - m^2_{2a}\right)}{E^2_{\rm cm}}\right)\boldsymbol{d}\,. \tag{22}$$

The total lab-frame energy E is related to the scattering K-matrix through the quantization condition

$$\det\left(1 - B^{(\boldsymbol{P})}\widetilde{K}\right) = \det\left(1 - \widetilde{K}B^{(\boldsymbol{P})}\right) = 0\,, \qquad \det\left(\widetilde{K}^{-1} - B^{(\boldsymbol{P})}\right) = 0\,. \tag{23}$$

The *box matrix* is given by

$$\begin{aligned}\langle J' m_{J'} L' S' a'|\; B^{(\boldsymbol{P})}\; |J m_J L S a\rangle \;=\; & -i\delta_{a'a}\delta_{S'S}\; q^{L'+L+1}_{{\rm cm},a}\; W^{(\boldsymbol{P}a)}_{L' m_{L'};\; L m_L} \\ & \times \langle J' m_{J'}|L' m_{L'}, S m_S\rangle\langle L m_L, S m_S|J m_J\rangle\,.\end{aligned} \tag{24}$$

This box matrix $B^{(\boldsymbol{P})}$ is Hermitian for $q^2_{{\rm cm},a}$ real, and the determinants in Eq. (23) are real. The $\langle j_1 m_1 j_2 m_2|JM\rangle$ are the familiar Clebsch–Gordan coefficients, and the $W^{(\boldsymbol{P}a)}$ matrix elements are given by

$$\begin{aligned}-iW^{(\boldsymbol{P}a)}_{L' m_{L'};\; L m_L} \;=\; & \sum_{l=|L'-L|}^{L'+L}\;\sum_{m=-l}^{l} \frac{\mathcal{Z}_{lm}\left(\boldsymbol{s}_a, \gamma, u^2_a\right)}{\pi^{3/2}\gamma u_a^{l+1}}\sqrt{\frac{(2L'+1)\,(2l+1)}{(2L+1)}} \\ & \times \langle L'0, l0|L0\rangle\langle L' m_{L'}, lm|L m_L\rangle\,.\end{aligned} \tag{25}$$

The Rummukainen–Gottlieb–Lüscher (RGL) shifted zeta functions are evaluated using

$$\begin{aligned}\mathcal{Z}_{lm}\left(\boldsymbol{s}, \gamma, u^2\right) = & \sum_{\boldsymbol{n}\in\boldsymbol{Z}^3} \frac{\mathcal{Y}_{lm}(\boldsymbol{z})}{(\boldsymbol{z}^2 - u^2)}{\rm e}^{-\Lambda\left(\boldsymbol{z}^2 - u^2\right)} + \delta_{l0}\frac{\gamma\pi}{\sqrt{\Lambda}}F_0\left(\Lambda u^2\right) \\ & + \frac{i^l\gamma}{\Lambda^{l+1/2}}\int_0^1 {\rm d}t\left(\frac{\pi}{t}\right)^{l+3/2}{\rm e}^{\Lambda t u^2}\sum_{\substack{\boldsymbol{n}\in\boldsymbol{Z}^3\\ \boldsymbol{n}\neq 0}}{\rm e}^{\pi i\boldsymbol{n}\cdot\boldsymbol{s}}\mathcal{Y}_{lm}(\boldsymbol{w})\;{\rm e}^{-\pi^2\boldsymbol{w}^2/(t\Lambda)}\,,\end{aligned} \tag{26}$$

where $\boldsymbol{z} = \boldsymbol{n} - \gamma^{-1}[\frac{1}{2} + (\gamma - 1)s^{-2}\boldsymbol{n}\cdot\boldsymbol{s}]\boldsymbol{s}$ and $\boldsymbol{w} = \boldsymbol{n} - (1-\gamma)s^{-2}\boldsymbol{s}\cdot\boldsymbol{n}\boldsymbol{s}$, the spherical harmonic polynomials are given by $\mathcal{Y}_{lm}(\boldsymbol{x}) = |\boldsymbol{x}|^l\, Y_{lm}(\widehat{\boldsymbol{x}})$, and

$$F_0(x) = -1 + \frac{1}{2}\int_0^1 \mathrm{d}t\ \frac{\mathrm{e}^{tx} - 1}{t^{3/2}}\,. \tag{27}$$

We choose $\Lambda \approx 1$ which allows for sufficient convergence speed of the summations.

To use the determinants in Eq. (23) in practice, we transform them to a block-diagonal basis and truncate in orbital angular momentum. Matrices corresponding to symmetry operations in the little group of $\boldsymbol{P}$ commute with the box matrix, leading to block-diagonal basis states

$$|\Lambda\lambda n J L S a\rangle = \sum_{m_J} c_{m_J}^{J(-1)^L;\,\Lambda\lambda n} |J m_J L S a\rangle\,, \tag{28}$$

where Λ denotes an irrep of the little group, λ labels the row of the irrep, and n is an occurrence index. The transformation coefficients depend on J and $(-1)^L$, but not on S, a. In this block-diagonal basis, the box matrix and the $\widetilde{K}$ matrix for $(-1)^{L+L'} = 1$ have the forms

$$\begin{aligned}
\langle \Lambda'\lambda' n' J' L' S' a'|\ B^{(\boldsymbol{P})}\ |\Lambda\lambda n J L S a\rangle &= \delta_{\Lambda'\Lambda}\delta_{\lambda'\lambda}\delta_{S'S}\delta_{a'a}\ B^{(\boldsymbol{P}\Lambda_B S a)}_{J'L'n';\ JLn}(E_{\mathrm{cm}})\,,\\
\langle \Lambda'\lambda' n' J' L' S' a'|\ \widetilde{K}\ |\Lambda\lambda n J L S a\rangle &= \delta_{\Lambda'\Lambda}\delta_{\lambda'\lambda}\delta_{n'n}\delta_{J'J}\ \widetilde{K}^{(J)}_{L'S'a';\ LSa}(E_{\mathrm{cm}})\,.
\end{aligned}$$

To eliminate any dependence on the truncation in orbital angular momentum, one can keep increasing the maximum retained L until the results converge.

The determinant in Eq. (23) is not a good quantity in which to search for zeros since it can vary rapidly and can become very large in magnitude. Furthermore, the box matrix is divergent at all of the non-interacting two-particle energies. When computing bootstrap errors, some of resamplings can cross these singularities, dramatically magnifying statistical errors. More importantly, when interactions are fairly weak in a scattering process, the required solutions of the quantization condition can occur uncomfortably close to these non-interacting energies where the divergences occur, making root finding to locate the zeros difficult.

The problem of the determinant becoming very large in magnitude is straightforward to deal with. Expressing the quantization condition in terms of the determinant is just a convenient way of saying that one eigenvalue becomes zero. One obvious way to proceed is to simply search for the zeros in each of the eigenvalues. Alternatively, consider the following function

of matrix A which appropriately rescales the determinant using a scalar parameter $\mu \neq 0$

$$\Omega(\mu, A) \equiv \frac{\det(A)}{\det\left[(\mu^2 + AA^\dagger)^{1/2}\right]}\,. \tag{29}$$

To evaluate this function, one first finds the eigenvalues $\lambda_\alpha(A)$ of A, then

$$\Omega(\mu, A) = \prod_k \frac{\lambda_k(A)}{(\mu^2 + |\lambda_k(A)|^2)^{1/2}}\,. \tag{30}$$

Clearly, when one of the eigenvalues is zero, this function is also zero. For eigenvalues which are much smaller than $|\mu|$, the associated term in the product tends towards the eigenvalue itself, divided by $|\mu|$. However, the key feature of this function is that for the eigenvalues which are much larger than $|\mu|$, the associated term in the product goes to $\mathrm{e}^{i\theta}$ for real θ. This function replaces the large eigenvalues with unimodular quantities so that the product should never overflow. This is a much better behaved function which still reproduces the quantization condition. As far as the quantization condition cares, the choice of μ is irrelevant.

The use of a Cayley transform solves the problem of the singularities in the box matrix. If we introduce the following Cayley transforms:

$$C_B^{(\boldsymbol{P})} = \left(1 + iB^{(\boldsymbol{P})}\right)\left(1 - iB^{(\boldsymbol{P})}\right)^{-1} = \left(1 - iB^{(\boldsymbol{P})}\right)^{-1}\left(1 + iB^{(\boldsymbol{P})}\right)\,, \tag{31}$$

$$\begin{aligned}\widetilde{S} &= \left(1 + i\widetilde{K}\right)\left(1 - i\widetilde{K}\right)^{-1} = \left(1 - i\widetilde{K}\right)^{-1}\left(1 + i\widetilde{K}\right) \\ &= -\left(1 - i\widetilde{K}^{-1}\right)\left(1 + i\widetilde{K}^{-1}\right)^{-1}\,,\end{aligned} \tag{32}$$

then a tamed quantization condition can be obtained

$$\det\left(1 + \widetilde{S}C_B^{(\boldsymbol{P})}\right) = 0\,, \qquad \det\left(\widetilde{S}^{-1} + C_B^{(\boldsymbol{P})}\right) = 0\,. \tag{33}$$

This determinant is no longer real, so both the real and imaginary parts must be combed for zeros. The Ω function can still be applied.

Each quantization condition in Eqs. (23) or (33) is a single relation between an energy E determined in a finite volume and the entire K-matrix. When multiple partial waves or multiple channels are involved, this relation is clearly not sufficient to extract all of the K-matrix elements at the single energy E. The best way to proceed is to approximate the K-matrix elements using physically motivated functions of the energy E_{cm} involving a handful of parameters. Values of these parameters can then be estimated by appropriate fits using a sufficiently large number of different energies.

3. The Δ resonance

One of the simplest baryon resonances to study in lattice QCD is the Δ resonance, which is an important feature of nucleon–pion scattering. Our most recent study of $N\pi$ scattering at $m_\pi \sim 200$ MeV was presented in Ref. [24]. Our results were obtained using 2000 configurations with four source times for the quark propagators of the CLS D200 ensemble, which uses a $64^3 \times 128$ lattice with spacing $a \sim 0.065$ fm and open boundary conditions in time. The quark masses are tuned such that $m_\pi \sim 200$ MeV and $m_K \sim 480$ MeV. The results for the finite-volume energies we obtained are shown in Fig. 3.

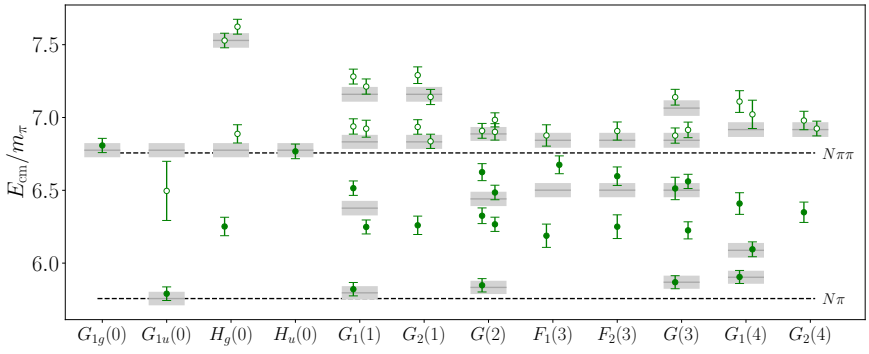

(a) The $I = 3/2$ spectrum.

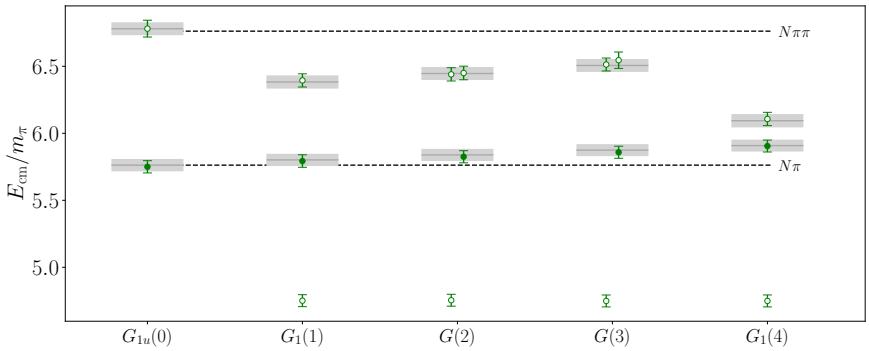

(b) The $I = 1/2$ spectrum.

Fig. 3. The low-lying $I = 3/2$ (top) and $I = 1/2$ (bottom) nucleon–pion spectra in the center-of-momentum frame on the D200 ensemble as energies over the pion mass from Ref. [24]. Each column corresponds to a particular irrep Λ of the little group of total momentum $\boldsymbol{P}^2 = (2\pi/L_b)^2\boldsymbol{d}^2$, denoted $\Lambda(\boldsymbol{d}^2)$. Dashed lines indicate the boundaries of the elastic region. Solid lines and shaded regions indicate non-interacting $N\pi$ levels and their associated statistical errors.

The goal of this analysis is a parametrization of the $J^P = 1/2^-$ partial wave for both isospins, and the $3/2^+$ wave with $I = 3/2$. Each partial wave is parametrized using the effective range expansion. For the $I = 3/2$, $J^P = 3/2^+$ wave, the next-to-leading order is included

$$\frac{q_{\rm cm}^3}{m_\pi^3} \cot \delta_{3/2^+} = \frac{6\pi\sqrt{s}}{m_\pi^3 g_{\Delta,\rm BW}^2} \left(m_\Delta^2 - s\right) , \tag{34}$$

where $\sqrt{s} = E_{\rm cm} = \sqrt{m_\pi^2 + q_{\rm cm}^2} + \sqrt{m_N^2 + q_{\rm cm}^2}$, and the effective range fit parameters are reorganized to form the conventional Breit–Wigner properties of the Δ resonance, denoted $g_{\Delta,\rm BW}^2$ and m_Δ. For the other waves, the leading term in the effective range expansion is sufficient

$$\frac{q_{\rm cm}^{2L+1}}{m_\pi^{2L+1}} \cot \delta_{J^P}^I = \frac{\sqrt{s}}{m_\pi A_{J^P}^I} , \tag{35}$$

where the overall $\sqrt{s}$ factors are adopted from standard continuum analysis, and the single fit parameter $A_{J^P}^I$ is trivially related to the scattering length

$$m_\pi^{2L+1} a_{J^P}^I = \frac{m_\pi}{m_\pi + m_N} A_{J^P}^I . \tag{36}$$

For the $(2J, L) = (3, 1)$ wave, energies in the $H_g(0)$, $G_2(1)$, $F_1(3)$, $G_2(4)$ irrep were used. In each irrep label, the integer in parentheses indicates $\boldsymbol{d}^2$, for total momentum $\boldsymbol{P} = 2\pi \boldsymbol{d}/L_b$. The $G_{1u}(0)$ irrep gives the $(1, 0)$ wave, the irreps used with s- and p-wave mixing were $G_1(1)$, $G(2)$, $G_1(4)$. The scattering phase shifts obtained from the finite-volume energies using the Lüscher quantization condition are shown in Fig. 4. For the Δ mass and Breit–Wigner width parameter $g_{\Delta,\rm BW}$, as well as the scattering lengths, the following results were obtained:

$$\begin{aligned} m_\Delta/m_\pi &= 6.290(18) , & g_{\Delta,\rm BW} &= 14.7(7) , \\ m_\pi a_0^{3/2} &= -0.2735(81) , & m_\pi a_0^{1/2} &= 0.142(22) . \end{aligned} \tag{37}$$

The amplitudes are well-described by the effective range expansion.

A comparison to chiral perturbation theory is presented in Ref. [24]. Not only do our results disagree with leading-order chiral perturbation theory (LO χPT), but we find that the magnitude of $m_\pi a_0^{3/2}$ is larger than that of $m_\pi a_0^{1/2}$, in disagreement with both LO χPT and phenomenology. For more details, see Ref. [24].

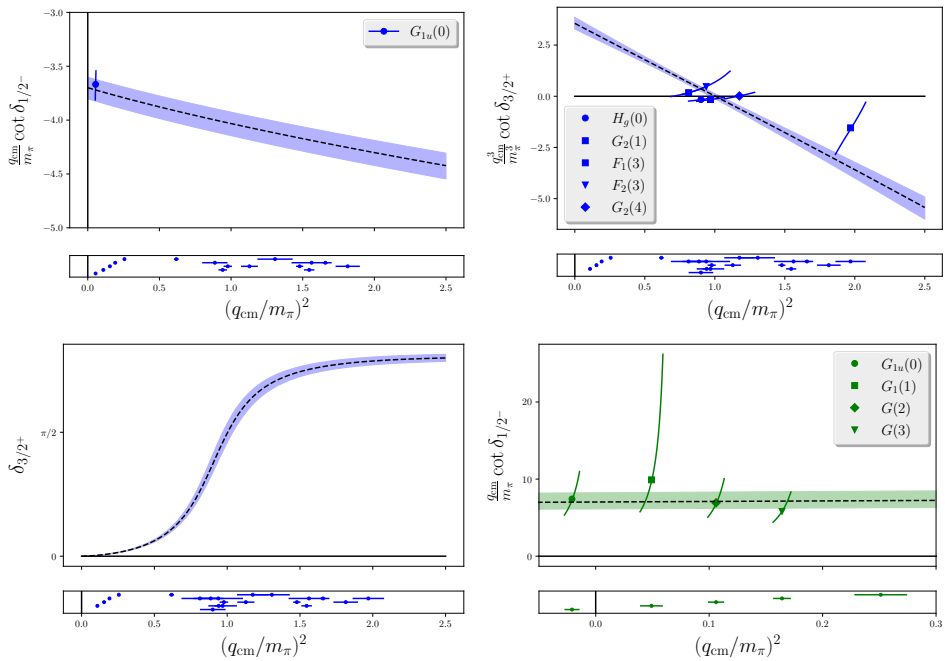

Fig. 4. $N\pi$ scattering phase shifts from Ref. [24] for $I = 3/2$ s-wave (top left) and p-wave (top right) in their cotangent form multiplied by threshold momentum factors. The p-wave phase shift itself is shown in the bottom left. Similarly, $N\pi$ scattering phase shifts for $I = 1/2$ s-wave (bottom right). Lower panels indicate all of the energies used in the fits to obtain the phase shifts in the top panels.

A more recent study of the Δ resonance at the physical point (with quark masses set to give the physical pion and kaon masses) and lattice spacing $a = 0.08$ fm was recently presented in Ref. [25]. Their finite-volume spectrum and scattering phase shift are shown in Fig. 5. Low three-particle thresholds were a problem in this study. The Δ resonance mass and width were found to be

$$\begin{aligned} M_{\rm R} &= 1269\,(39)_{\rm stat}(45)_{\rm total}\ {\rm MeV}\,, \\ \Gamma_{\rm R} &= 144\,(169)_{\rm stat}(181)_{\rm total}\ {\rm MeV}\,. \end{aligned}$$

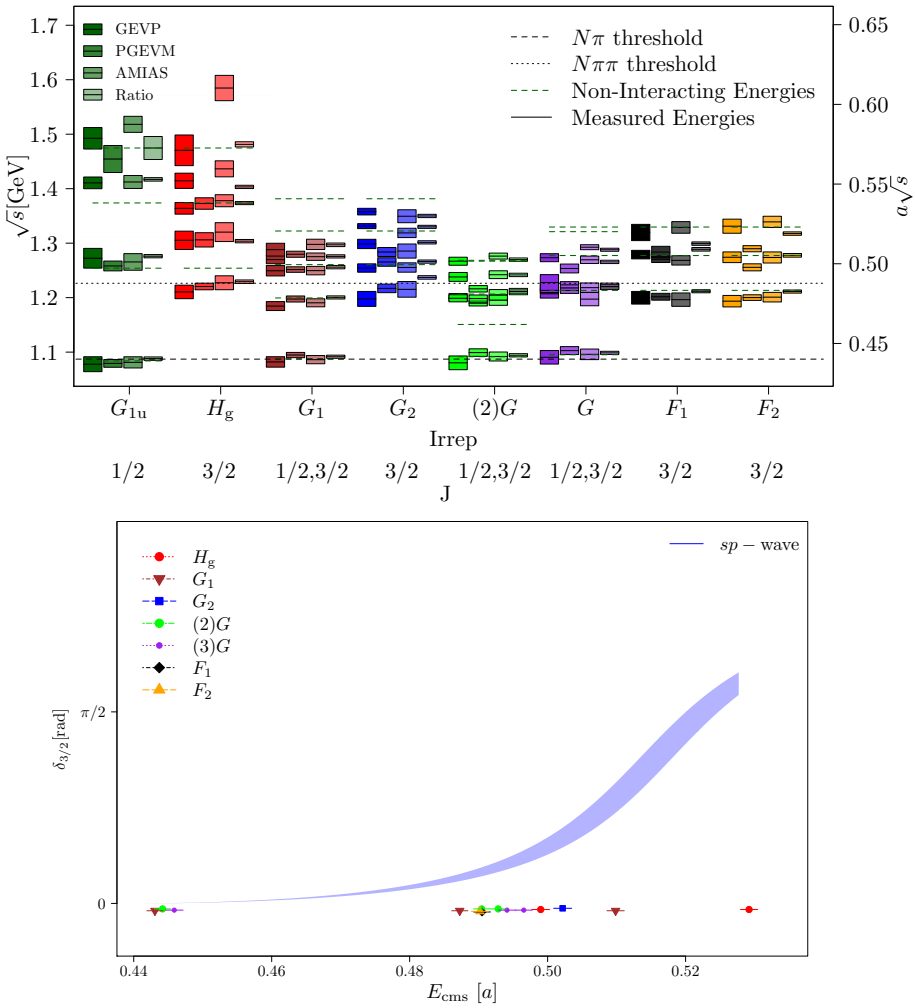

Fig. 5. Top: The πN interacting two-hadron energy levels obtained in Ref. [25]. Box heights indicate estimated uncertainties. Horizontal dashed/dotted lines show various thresholds, as indicated by the legend. Non-interacting energies are shown by the green, thicker dashed lines. Bottom: The P-wave scattering phase-shift as a function of the invariant mass $E_{\rm cm} = \sqrt{s}$. The error band is determined using jackknife resampling. The points with horizontal error bars show each fitted energy level including its jackknife error bar.

4. Two-pole nature of scattering near the $\Lambda(1405)$

An interesting energy region to probe for resonances having non-zero strangeness is in the vicinity of the puzzling $\Lambda(1405)$ resonance. Our recent

study of $\Sigma\pi$ and $N\bar{K}$ scattering in the $\Lambda(1405)$ energy region was presented in Refs. [26, 27]. Our results, shown in Fig. 6, were obtained using the CLS D200 ensemble with $m_\pi \sim 200$ MeV. This was the first lattice QCD study of this system to include both single-hadron and all needed two-hadron operators to carry out a full coupled-channel analysis.

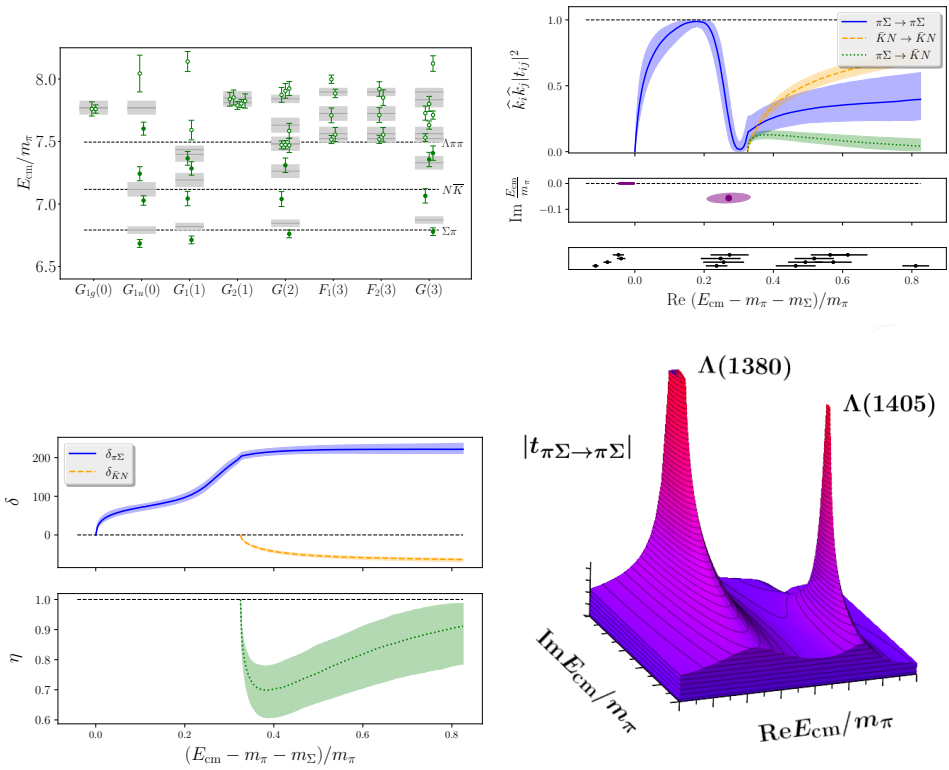

Fig. 6. Top left: Finite volume energy spectrum involving interacting $\Sigma\pi$ and $N\bar{K}$ states as ratios over the pion mass from Refs. [26, 27]. Green symbols are our results, gray bands show non-interacting energies. Labels on the horizontal axis show the irreps $\Lambda(\boldsymbol{d}^2)$ for lab-frame total momenta $\boldsymbol{P} = (2\pi/L)\boldsymbol{d}$, where $\boldsymbol{d}$ is a three-vector of integers and the lattice spatial volume is L^3. Top right: Upper panel shows the isoscalar, strangeness -1, $i \to j$ transition amplitudes squared for $i, j = \Sigma\pi, N\bar{K}$; middle panel shows positions of the S-matrix poles in the complex center-of-mass energy plane on the sheet closest to the physical one; bottom panel shows the finite-volume energies used in the fit. Bottom left: Inelasticity η and phase shifts $\delta_{\pi\Sigma}$ and $\delta_{\bar{K}N}$. Bottom right: Three-dimensional plot of the $\Sigma\pi \to \Sigma\pi$ transition amplitude magnitude showing the two poles.

The energies of the finite-volume stationary states we obtained are shown in the upper left-hand plot of Fig. 6. An effective range expansion with $L_{\max} = 0$ of the form

$$\frac{E_{\rm cm}}{M_\pi}\widetilde{K}_{ij} = A_{ij} + B_{ij}\Delta_{\pi\Sigma}\,, \tag{38}$$

$$\Delta_{\pi\Sigma} = \left(E_{\rm cm}^2 - (M_\pi + M_\Sigma)^2\right) \Big/ (M_\pi + M_\Sigma)^2\,, \tag{39}$$

where A_{ij} and B_{ij} are symmetric and real coefficients with i and j denoting either of the two scattering channels, provided the best description of the data, but several other parametrizations were also used, including an ERE for $\widetilde{K}^{-1}$, the form above with the outer factor of $E_{\rm cm}$ removed, and a Blatt–Biedenharn form. The fit with the lowest AIC value is a four-parameter fit of the form of Eq. (39), and the best-fit parameter values are

$$\begin{aligned} A_{00} &= 4.2(1.8)\,, & A_{11} &= -10.4(1.1)\,, \\ A_{01} &= 10.4(1.6)\,, & B_{01} &= -30(18)\,, \end{aligned} \tag{40}$$

with fixed $B_{00} = B_{11} = 0$ and $\chi^2 = 11.17$ for 11 degrees of freedom. This fit is shown in Fig. 6. All statistical uncertainties and correlations for this fit are taken into account using the bootstrap method with 800 samples.

To study the scattering amplitudes, we define a quantity $t_{ij}^{(J^P)}(E_{\rm cm})$ which is proportional to the scattering transition amplitude and is related to $\widetilde{K}$ by

$$t^{-1} = \widetilde{K}^{-1} - i\widehat{k}\,, \tag{41}$$

where $\widehat{k} = \mathrm{diag}(k_{\pi\Sigma}, k_{\bar{K}N})$, with

$$k_{\pi\Sigma}^2 = \frac{1}{4E_{\rm cm}^2}\lambda_{\rm K}\left(E_{\rm cm}^2, m_\pi^2, m_\Sigma^2\right)\,, \tag{42}$$

$$k_{\bar{K}N}^2 = \frac{1}{4E_{\rm cm}^2}\lambda_{\rm K}\left(E_{\rm cm}^2, m_{\bar{K}}^2, m_N^2\right)\,, \tag{43}$$

and $\lambda_{\rm K}$ is the Källén function [28]

$$\lambda_{\rm K}(x,y,z) = x^2 + y^2 + z^2 - 2xy - 2xz - 2yz\,. \tag{44}$$

The results for the scattering transition amplitudes are shown in the upper right panel of Fig. 6, and the pole locations for each of the fits are shown in the lower right panel of Fig. 6. Our fits to the transition amplitudes revealed a two-pole structure, with locations

$$E_1 = 1395(9)(2)(16)\ \text{MeV}\,, \tag{45}$$

$$E_2 = [1456(14)(2)(16) - i\,11.7(4.3)(4)(0.1)]\ \text{MeV}\,, \tag{46}$$

with the first uncertainty being statistical, the second coming from our different parametrizations of the amplitudes, and the third arising from scale setting. A virtual bound state below the $\Sigma\pi$ threshold was found, as well as a resonance pole below the $N\bar{K}$ threshold. Fit forms with just one pole were tried and all were strongly disfavored. The two-pole structure in the $\Lambda(1405)$ region was first suggested in Ref. [29]. The scattering phase shifts δ_i and the inelasticity η are related to t by

$$t_{00} = \frac{\eta\, e^{2i\delta_{\pi\Sigma}} - 1}{2i\widehat{k}_{\pi\Sigma}}, \tag{47}$$

$$t_{11} = \frac{\eta\, e^{2i\delta_{\bar{K}N}} - 1}{2i\widehat{k}_{\bar{K}N}}, \tag{48}$$

$$t_{01} = \frac{\sqrt{1-\eta^2}\, e^{i(\delta_{\pi\Sigma}+\delta_{\bar{K}N})}}{2\sqrt{\widehat{k}_{\pi\Sigma}\widehat{k}_{\bar{K}N}}}, \tag{49}$$

where the indices indicate the flavor channel: 0 for $\pi\Sigma$ and 1 for $\bar{K}N$. The results are shown in the lower left panel of Fig. 6.

The analysis above only includes S-waves and the $J^P = 1/2^-$ amplitudes. The energies in non-zero momentum frames, such as the $G_1(1)$, $G(2)$, and $G(3)$ irreps, receive contamination from P-waves. To assess the importance of such contributions, additional fits with a very simple parametrization for the higher partial waves were done. The effects of the higher partial waves were found to be negligible for energies below the $\Lambda\pi\pi$ threshold.

5. The Roper resonance

The first excitation of the proton, known as the Roper resonance, is an important resonance. Experimentally, it is a 4-star resonance $N(1440)$ with $I(J^P) = \frac{1}{2}(\frac{1}{2}^+)$ and a width in the range of 250–450 MeV. It is a notoriously difficult resonance to study in lattice QCD. Local three-quark operators have difficulty capturing the Roper level near 1.4 GeV and instead create a state with an energy much higher near 2.0 GeV. This fact is illustrated in the upper plot of Fig. 7 which shows energy extractions for the proton and its first excitation from three lattice QCD studies.

The Roper resonance was studied in Ref. [34] using only a selection of three-quark operators with domain-wall fermions in the sea and overlap fermions for the valence quarks. Their results, shown in the lower panel in Fig. 7, are obtained employing a large basis of three-quark operators with different quark-field smearings and a sequential empirical Bayesian analysis method. The Roper mass does seem to be captured, but with very large uncertainties.

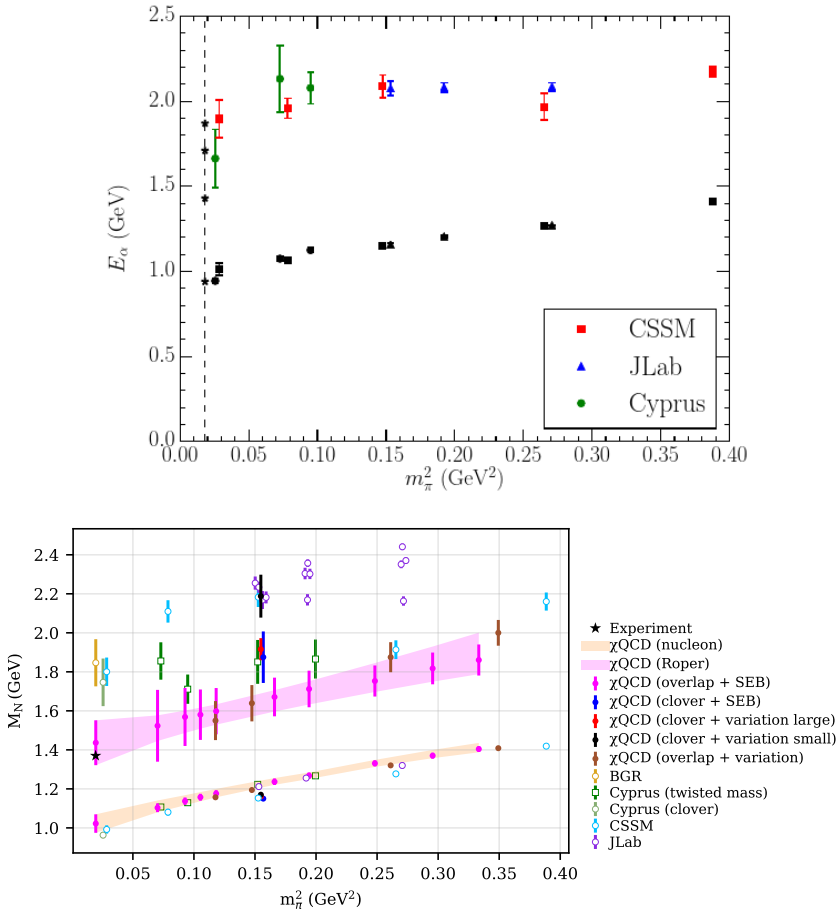

Fig. 7. Top: Current status of positive-parity excitations of the proton from Ref. [30] which compares results from Refs. [31–33]. Such studies which only use three-quark operators miss the Roper and instead capture a higher lying excitation. Bottom: Results for the positive-parity excitation spectrum of the proton from Ref. [34] are shown. A large number of differently-smeared three-quark operators, combined with a domain-wall fermion sea, overlap valence fermions, and a sequential Bayesian analysis method, seems to capture the Roper (magenta band), but with rather large uncertainties.

It is evident that a definitive study of the Roper resonance needs multi-hadron operators involving $N\pi$, $N\sigma$, $\Delta\pi$ operators, as well as $N\pi\pi$ operators. Large volumes will be needed, as well as a three-particle amplitude analysis, which has become available only recently [35].

6. Conclusion

Recent innovations in the lattice QCD methods, such as the stochastic LapH method and distillation, have facilitated reliable determinations of energies involving multi-hadron states. Large numbers of excited-state energy levels can now be estimated, allowing scattering phase shifts to be computed and hadron resonance properties, such as masses and decay widths, to be determined. Our recent results for the Δ and $\Lambda(1405)$ resonances from lattice QCD were highlighted. The famous Roper resonance is still a challenge, but future studies involving three-particle operators may finally shed light on this elusive hadron.

The works described here were done in collaboration with John Bulava, Bárbara Cid-Mora, Andrew D. Hanlon, Ben Hörz, Daniel Mohler, Joseph Moscoso, Amy Nicholson, Fernando Romero-López, Sarah Skinner, Pavlos Vranas, and André Walker-Loud. The author gratefully acknowledges support from the U.S. National Science Foundation (NSF) under awards PHY-2209167 and PHY-2514831. Computations were carried out on Frontera [36] at the Texas Advanced Computing Center (TACC) under award PHY20009, and at the National Energy Research Scientific Computing Center (NERSC), the U.S. Department of Energy (DOE) Office of Science User Facility located at Lawrence Berkeley National Laboratory (LBNL), operated under contract No. DE-AC02-05CH11231 using NERSC awards NP-ERCAP0005287, NP-ERCAP0010836 and NP-ERCAP0015497.

REFERENCES

[1] H. Fritzsch, M. Gell-Mann, H. Leutwyler, «Advantages of the color octet gluon picture», *Phys. Lett. B* **47**, 365 (1973).

[2] L.D. Roper, «Evidence for a P_{11} Pion–Nucleon Resonance at 556 MeV», *Phys. Rev. Lett.* **12**, 340 (1964).

[3] K.G. Wilson, «Confinement of quarks», *Phys. Rev. D* **10**, 2445 (1974).

[4] N. Metropolis *et al.*, «Equation of State Calculations by Fast Computing Machines», *J. Chem. Phys.* **21**, 1087 (1953).

[5] M.A. Clark, A.D. Kennedy, «Accelerating Dynamical-Fermion Computations Using the Rational Hybrid Monte Carlo (Rhmc) Algorithm with Multiple Pseudofermion Fields», *Phys. Rev. Lett.* **98**, 051601 (2007).

[6] C. Morningstar, M.J. Peardon, «Analytic smearing of SU(3) link variables in lattice QCD», *Phys. Rev. D* **69**, 054501 (2004).

[7] Hadron Spectrum Collaboration (M. Peardon *et al.*), «Novel quark-field creation operator construction for hadronic physics in lattice QCD», *Phys. Rev. D* **80**, 054506 (2009).

[8] C. Morningstar *et al.*, «Improved stochastic estimation of quark propagation with Laplacian Heaviside smearing in lattice QCD», *Phys. Rev. D* **83**, 114505 (2011).

[9] G. Fox, R. Gupta, O. Martin, S. Otto, «Monte Carlo estimates of the mass gap of the O(2) and O(3) spin models in (1+1)-dimensions», *Nucl. Phys. B* **205**, 188 (1982).

[10] K. Ishikawa, M. Teper, G. Schierholz, «The glueball mass spectrum in QCD: First results of a lattice Monte Carlo calculation», *Phys. Lett. B* **110**, 399 (1982).

[11] C. Michael, I. Teasdale, «Extracting glueball masses from lattice QCD», *Nucl. Phys. B* **215**, 433 (1983).

[12] M. Lüscher, U. Wolff, «How to calculate the elastic scattering matrix in two-dimensional quantum field theories by numerical simulation», *Nucl. Phys. B* **339**, 222 (1990).

[13] M. Lüscher, «Two-particle states on a torus and their relation to the scattering matrix», *Nucl. Phys. B* **354**, 531 (1991).

[14] M. Lüscher, «Signatures of unstable particles in finite volume», *Nucl. Phys. B* **364**, 237 (1991).

[15] K. Rummukainen, S.A. Gottlieb, «Resonance scattering phase shifts on a non-rest-frame lattice», *Nucl. Phys. B* **450**, 397 (1995).

[16] C.H. Kim, C.T. Sachrajda, S.R. Sharpe, «Finite-volume effects for two-hadron states in moving frames», *Nucl. Phys. B* **727**, 218 (2005).

[17] R.A. Briceno, «Two-particle multichannel systems in a finite volume with arbitrary spin», *Phys. Rev. D* **89**, 074507 (2014).

[18] C. Morningstar *et al.*, «Estimating the two-particle K-matrix for multiple partial waves and decay channels from finite-volume energies», *Nucl. Phys. B* **924**, 477 (2017).

[19] E.P. Wigner, «Resonance Reactions and Anomalous Scattering», *Phys. Rev.* **70**, 15 (1946).

[20] E.P. Wigner, L. Eisenbud, «Higher Angular Momenta and Long Range Interaction in Resonance Reactions», *Phys. Rev.* **72**, 29 (1947).

[21] M.H. Ross, G.L. Shaw, «Multichannel effective range theory», *Ann. Phys.* **13**, 147 (1961).

[22] J. de Swart, C. Dullemond, «Effective range theory and the low energy hyperon–nucleon interactions», *Ann. Phys.* **19**, 458 (1962).

[23] P.G. Burke, «Chapter 3: Resonances and Threshold Behaviour», in: «R-matrix Theory of Atomic Collisions: Application to Atomic, Molecular and Optical Processes», *Springer*, Heidelberg 2011, pp. 135–139.

[24] J. Bulava *et al.*, «Elastic nucleon–pion scattering at $m_\pi = 200$ MeV from lattice QCD», *Nucl. Phys. B* **987**, 116105 (2023).

[25] C. Alexandrou *et al.*, «Elastic nucleon–pion scattering amplitudes in the Δ channel at physical pion mass from lattice QCD», *Phys. Rev. D* **109**, 034509 (2024).

[26] Baryon Scattering (BaSc) Collaboration (J. Bulava *et al.*), «Two-Pole Nature of the $\Lambda(1405)$ Resonance from Lattice QCD», *Phys. Rev. Lett.* **132**, 051901 (2024).

[27] Baryon Scattering (BaSc) Collaboration (J. Bulava *et al.*), «Lattice QCD study of $\pi\Sigma$–$\bar{K}N$ scattering and the $\Lambda(1405)$ resonance», *Phys. Rev. D* **109**, 014511 (2024).

[28] G. Källén, «Elementary Particle Physics», *Addison-Wesley*, Reading, MA 1964.

[29] J.A. Oller, U.G. Meißner, «Chiral dynamics in the presence of bound states: kaon–nucleon interactions revisited», *Phys. Lett. B* **500**, 263 (2001).

[30] D. Leinweber, «Physical Interpretation of the Baryon Spectrum», in: «Proceedings of the 14$^{\text{th}}$ International Workshop on the Physics of Excited Nucleons», York, UK, 17–21 June, 2024.

[31] C. Alexandrou, T. Leontiou, C.N. Papanicolas, E. Stiliaris, «Novel analysis method for excited states in lattice QCD: The nucleon case», *Phys. Rev. D* **91**, 014506 (2015).

[32] R.G. Edwards, J.J. Dudek, D.G. Richards, S.J. Wallace, «Excited state baryon spectroscopy from lattice QCD», *Phys. Rev. D* **84**, 074508 (2011).

[33] Z.-W. Liu *et al.*, «Hamiltonian effective field theory study of the $N^*(1440)$ resonance in lattice QCD», *Phys. Rev. D* **95**, 034034 (2017).

[34] χQCD Collaboration (M. Sun *et al.*), «Roper state from overlap fermions», *Phys. Rev. D* **101**, 054511 (2020).

[35] M.T. Hansen, F. Romero-López, S.R. Sharpe, «Finite-volume formalism for $N\pi\pi$ at maximal isospin», arXiv:2509.24778 [hep-lat].

[36] D. Stanzione *et al.*, «Frontera: The Evolution of Leadership Computing at the Texas Advanced Computing Center», in: «Proceedings of Practice and Experience in Advanced Research Computing 2020: Catch the Wave, PEARC'20», *Association for Computing Machinery, New York*, NY, USA, 27–31 July, 2020, pp. 106–111.